Fast Charging Capability of Thin-Film Prussian Blue Analogue Electrodes for Aqueous Sodium-Ion Batteries

Xaver Lamprecht[a], Philipp Zellner[a], Göktug Yesilbas[a], Ludek Hromadko[b,c], Philipp Moser[a], Philipp Marzak[a], Shujin Hou[a], Richard Haid[a], Florian Steinberger[a], Tim Steeger[a], Jan M. Macak[b,c], Aliaksandr S. Bandarenka*[,a]

(a) Physics of Energy Conversion and Storage, Physik-Department, Technische Universität München, James-Franck-Str. 1, 85748 Garching bei München, Germany

(b) Central European Institute of Technology, Brno University of Technology, Purkynova 123, 61200, Brno, Czech Republic

(c) Center of Materials and Nanotechnologies, Faculty of Chemical Technology, University of Pardubice, Nam.Cs.Legii 565, 53002 Pardubice, Czech Republic

*Corresponding Author E-mail: bandarenka@ph.tum.de

ABSTRACT

Prussian Blue Analogues (PBA) are considered as promising candidates for aqueous sodium-ion batteries providing a sufficiently high energy density for stationary energy storage. However, suppose the operation of such materials under high-power conditions could be facilitated. In that case, their application might involve fast-response power grid stabilization and enable short-distance urban mobility due to fast re-charging. In this work, nickel hexacyanoferrate thin-film electrodes are synthesized *via* a facile electrochemical deposition approach, and their fast-charging capability is systematically investigated with regard to the electroactive material thickness. Whereas kinetics allows an extremely fast (dis)charging within a few seconds for sub-micron film thicknesses, a transition towards mass transfer control is observed when further increasing the rate. This can be entirely attributed to the limiting effects of solid-state diffusion of Na^+ within the electrode material. This work highlights a possible pathway towards hybrid battery-supercapacitor systems by presenting a PBA model cell yielding 25 Wh/kg at up to 10 kW/kg.

TOC FIGURE

To be done

KEYWORDS

Na-ion aqueous batteries; Prussian blue analogs; sodium nickel hexacyanoferrate; fast-charging capability; thin-film electrochemical deposition; hybrid battery-supercapacitor

INTRODUCTION

Over the last years, rechargeable batteries have become regarded as an essential enabler for the transition of the world's energy provision scheme towards sustainability. Today, the market is dominated by "traditional" lithium-ion batteries due to the demand for high energy densities in electric vehicles.[1,2] However, alternative battery technologies are inevitably needed, especially considering the increasing adoption of stationary energy storage applications in the power grid, where resource availability, safety, and durability outweigh energy density.[2,3,4,5] Aqueous sodium-ion batteries (ASIBs) could play a substantial role in replacing LIBs for such applications in the future.[6]

The material class of Prussian Blue Analogues (PBA) has gained increasing attention for being a promising candidate for scalable, cost-efficient, and ecologically friendly ASIB electrodes.[7,8,9,10] In general, the stoichiometry of these transition metal coordination compounds is described by $AM_xTM^{(1)}[TM^{(2)}(CN)_6]$, where AM is an alkali metal cation, like Li^+, Na^+ or K^+, and $TM^{(1,2)}$ are transition metals interconnected by cyanide ligands.[11] The AM-cations can reversibly intercalate into the PBA open-framework structure to compensate for the charge from the TM redox activity. Ionic charge propagation within the PBA lattice is enabled *via* solid-state diffusion along the wide channels of the nanoporous three-dimensional network.[11]

Whereas an extremely long cycle life of several thousand cycles is enabled by so-called water in salt electrolytes,[12,13] also decent energy densities in the order of 10s Wh/kg have been reported for entirely PBA-based ASIBs.[12,14,15] Traditionally, PBAs are synthesized *via* coprecipitation, followed by casting a slurry containing the active material powder, conductive carbon and a polymeric binder on a current collector to form a composite electrode.[7] Even though being the standard up-to-date method, it bears several disadvantages, such as holding a significant share of inactive material and impaired intercalation kinetics due to limited access

of ions to the active material surface.[16,17,18] Furthermore, without optimized and controlled synthesis conditions, the coprecipitation method commonly yields primary and secondary particles of imperfect and detrimental crystallinity and morphology.[19,20] These effects negatively impact the available capacity and give rise to a potential hysteresis of the electrodes when charged and discharged at high rates.

In contrast, binder-free nano/microstructured PBA electrodes can possibly hold great potential for high-rate ASIBs.[15,21,22,23] Such hybrid battery-supercapacitor systems, which combine a decent energy density with high power density, could not only serve the energy transition by stationary usage for fast-response power grid stabilization but also open opportunities for short-distance transportation use-cases like urban buses.[4,24,25,26] It has been known for over forty years, that microstructured thin-film PBA electrodes can be easily synthesized by a single-step electrodeposition process on top of a conductive template.[27,28,29] Yet, their performance as battery electrode material still requires reasonable benchmarking against the "classic" composite electrode configuration.[30] This work comprises a systematic study of the fast-charging capability of sodium nickel hexacyanoferrate (NiHCF) thin-film electrodes prepared *via* the electrodeposition method as a function of the mass loading and film thickness. The electrochemical behavior of the thin-film electrodes is compared to a composite-type one, and their performance is analyzed with regard to the rate-determining steps during the (dis)charging process. The findings are extrapolated to ASIB full-cell configurations by providing characterization data of two solely PBA-based systems. This report aims to provide an understanding of the potential benefits and open challenges for thin-film PBA electrodes.

EXPERIMENTAL

Preparation and Electrochemical Characterization of Battery Electrodes

Thin-film electrodes were prepared by direct electrodeposition, whereas bulky electrodes were obtained from active material powder via slurry casting. The two differing routines are presented in **Figure 1**. A list of used chemicals and their suppliers is provided in **Table S1**.

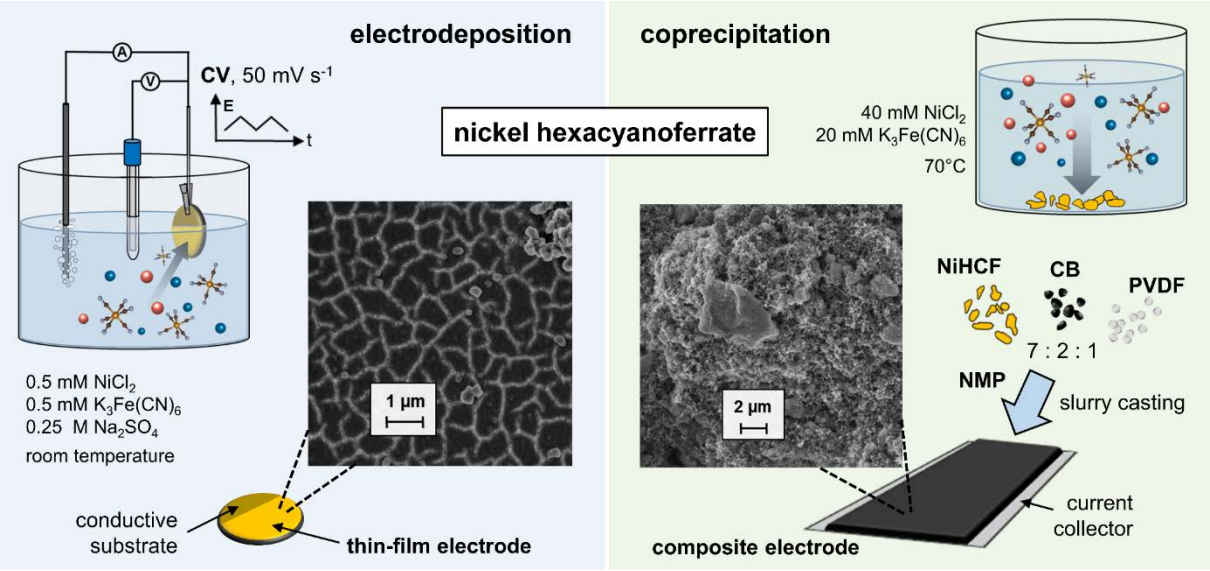

Figure 1. *Routines for the preparation of NiHCF electrodes. (**left**) Direct electrodeposition of pure active material thin films on a conductive substrate from an aqueous precursor solution. (**right**) Synthesis of NiHCF nanoparticles via coprecipitation. The active material is mixed with carbon black and a polymeric binder, followed by preparing a slurry with an organic solvent. A high-mass loading, porous composite electrode coating is obtained on the current collector.*

The electrodeposition of NiHCF was carried out in a three-electrode configuration in a custom glass setup under an argon atmosphere (5.0, *Westfalen AG*).[15] An Ag/AgCl (SSC, B3420+, *SI Analytics*) reference electrode was used along with a Pt wire as a counter electrode. 1.37 cm^2 gold-on-quartz crystals (in a QCM200 microbalance, AT-cut, Au on Ti adhesive layer, *Stanford Research Systems*) served as the substrates for determining the mass of deposited electrode material. Alternatively, gold-on-glass substrates (*Arrandee Metal*) were used to prepare

samples for the morphological and crystallographic examination. A VSP-300 potentiostat (*Bio-Logic*) was used to control and measure the electrode potentials and current.

Au substrates were rinsed with ultrapure water (18.2 MΩ, *Evoqua*), followed by a cleaning step using cyclic voltammetric (CV) scans (0 ↔ 1.3 V *vs*. SSC at 50 mV/s) in 0.1 M H_2SO_4 and rinsing with ultrapure water again. The electrodeposition method was adopted from refs [31,32], cycling the Au substrates (CV, 50 mV/s, 0 ↔ 0.9 V *vs*. SSC) in an aqueous precursor solution consisting of 0.5 mM $NiCl_2$, 0.5 mM $K_3Fe(CN)_6$, and 0.25 M Na_2SO_4. The latter served as a supporting electrolyte to guarantee sufficient ionic conductivity of the plating solution. The process was stopped after reaching the desired mass loading as obtained from the *in-operando* QCM measurement, terminating the CV scan at the lower potential vertex. As this yields a fully reduced electrode, the indicated mass loadings refer to intercalated NiHCF (i.e., $Na_2NiFe(CN)_6$). The samples were washed with argon-purged ultrapure water, followed by drying under a continuous argon stream for at least one hour.

Bulky electrodes with a mass loading of 1.49 mg/cm^2 (active material) were obtained following the routine as described by Wessells et al.[33] NiHCF nanoparticles were synthesized from an aqueous solution of 40 mM $NiCl_2$ and 20 mM $K_3Fe(CN)_6$ at 70°C under continuous stirring. The reagents were added dropwise in equal quantities from stock solutions, and the mixture was allowed to rest for 10 minutes. The orange precipitate was centrifuged, washed with ultrapure water several times, and dried at 70°C under ambient conditions. NiHCF electrodes were prepared by mixing the synthesized active material, carbon black, and PVDF in a 7:2:1 ratio, using NMP as a solvent, and coating the slurry on the stainless steel foil.

The electrochemical characterization of battery electrodes was performed under an argon atmosphere in the three-electrode setup described above with 8 M $NaClO_4$, as this water-in-salt electrolyte allows a degradation-free operation of the electrodes over long cycling intervals.[12,13] The measurement protocols involved CV scans at different rates and galvanostatic cycling with potential limitations at varying C-rates. Furthermore, staircase-potential electrochemical

impedance spectroscopy (EIS) was performed with a probing AC amplitude of 10 mV in a frequency range between 100 kHz and 100 mHz. System stationarity was guaranteed by an appropriate waiting period before the impedance spectra acquisition, and the validity of all data within the analysis interval was verified by the Kramers-Kronig check. The spectra were fitted using the software EIS Data Analysis 1.3[34] using the electrical equivalent circuit presented in the supporting information.

Full Cell Battery Assemblies

Full cell prototypes were assembled in the glass cell setup described in ref. [13]. The respective cathode and anode thin-film electrodes were previously electrodeposited on Au-QCM substrates. The experimental details for the preparation of sodium manganese hexacyanomanganate (MnHCM) and sodium cobalt hexacyanoferrate (CoHCF) are given in the supporting information. After the deposition of the individual cathode and anode thin-film electrodes, the respective glass cells were connected ionically by opening the closures of an electrolyte bridge. The large spatial distance between the cathode and anode results in a high uncompensated resistance across the electrolyte bridge of ~153.5 Ω in 8 M $NaClO_4$, as determined by EIS. As this setup allows the use of a reference electrode in the full cell configuration, the potential limits of the individual electrodes could be precisely controlled during cycling and were as follows: NiHCF [0.8 V ↔ 0.1 V *vs.* SSC] – MnHCM [-1.2 V ↔ -0.6 V *vs.* SSC] and CoHCF [1.2 V ↔ 0.6 V *vs.* SSC] – NiHCF [0.1 V ↔ 0.6 V *vs.* SSC].

Crystallographic and Morphological Characterization

The grazing incidence X-ray diffraction (XRD) pattern of the thin-film electrodes was acquired in the range of $2\vartheta = 5° – 65°$ (step size = 0.026°, incident angle 1°) using Panalytical Empyrean with a Cu tube (λ = 1.5406 Å, 45 kV, 40 mA) and a Pixcel3D detector. The powder XRD pattern of the synthesized NiHCF precipitate was collected on a Rigaku Miniflex (*Rigaku*) with a Ni-filtered Cu-Kα radiation (λ = 1.5406 Å). The procedure used for XRD measurements

consisted of a 2ϑ range from 10° to 62.5° and a slow-scanning step of 2° per minute. The simulated diffraction pattern was obtained by modeling $Na_2NiFe(CN)_6$ with a face-centered cubic $Fm\bar{3}m$ crystal structure (see **Figure S1**) and a lattice constant of 10.27 Å using the software VESTA (version 3.0).

The surface was scanned by atomic force microscopy (AFM) in tapping mode (scan rate 0.5 Hz) to evaluate the morphology of the films. For this purpose, an EC-STM/AFM Multimode device (*Veeco Instruments*) with a Nanoscope IIID controller and the Nanoscope 5.31r1 software was utilized. The AFM probes were made from silicon (RTESP-300, purchased from *Bruker*). The roughness of the surface was analyzed by using the WSxM software.[35]

Top-view and cross-section images of the thin films were obtained from a field-emission scanning electrode microscope (SEM, JSM-7500F, *JEOL*). Samples were prepared for cross-sectional imaging by mechanical rupture. All samples were directly visualized (i.e., without any coating to increase the samples' conductivity) using either in-lens (top-views) or lower (cross-sections) secondary electron detector. The morphologies of NiHCF powders were acquired on an NVision40 FESEM (*Zeiss*) with a working voltage of 5.0 kV and a working distance of 7.4 mm.

The thickness of the electrodeposited NiHCF thin films was determined using a DekTak profilometer (*Bruker*).

RESULTS & DISCUSSION

The electrodeposition method leads to a homogenous coating of the current collector with pure additive- and binder-free active material. In general, the deposition of NiHCF thin films from the available solvated precursor ions (Na^+, $Fe(CN)_6^{3-}$, Ni^{2+}) on the electrified substrate can follow two different pathways:[36] anodic, precipitation (chemical) on the substrate:

$$2Fe(CN)_6^{3-} + 3Ni^{2+} \rightarrow 2Ni_{1.5}Fe(CN)_6 \quad \text{(eq. 1)},$$

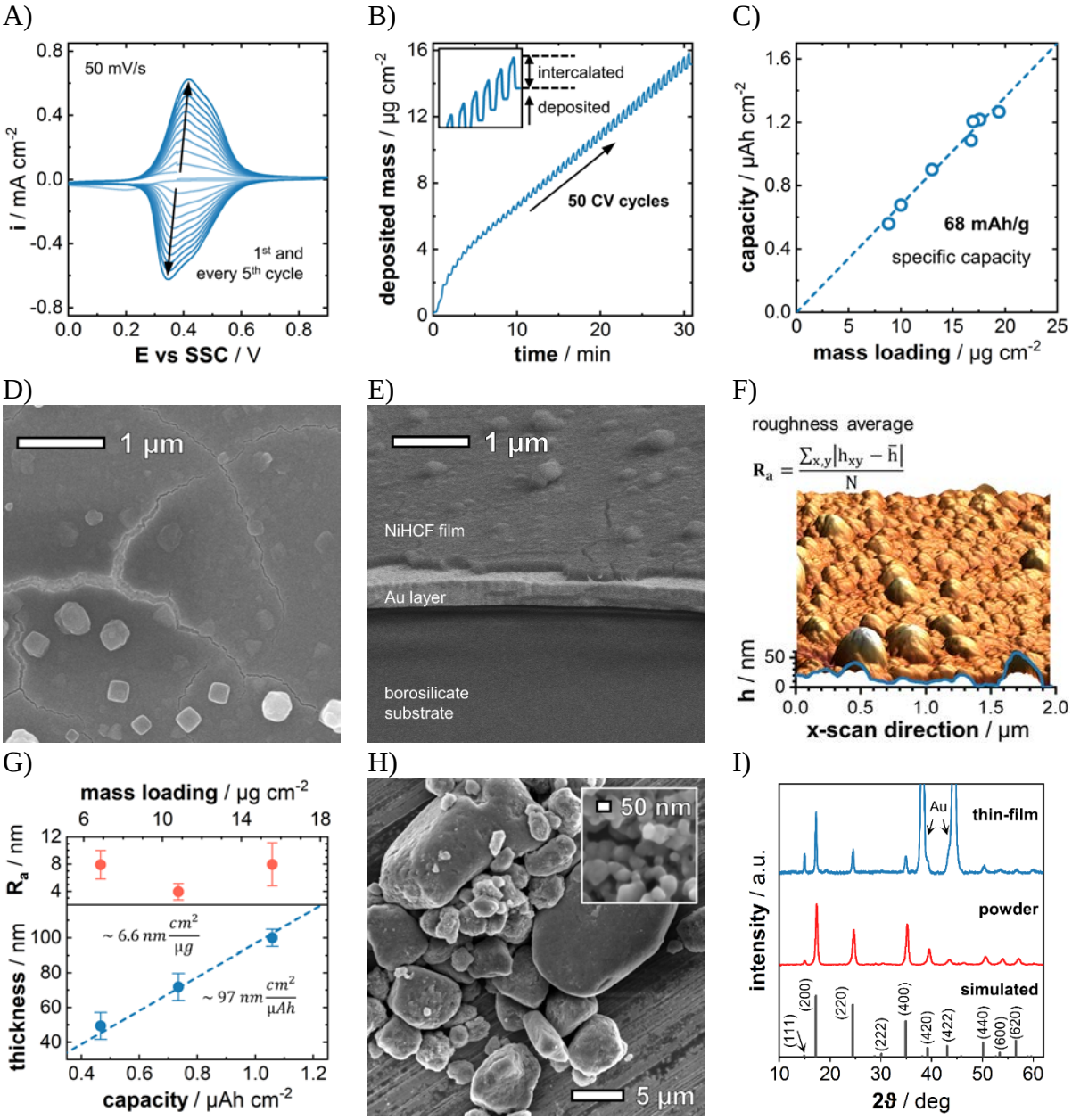

Figure 2. *(**A**) CVs showing the electrodeposition of a NiHCF thin film and (**B**) the corresponding deposited mass determined via EQCM on an Au substrate. (**C**) The areal capacity obtained for different mass loadings of electrodeposited thin film electrodes allows for the extraction of the specific capacity of NiHCF. (**D**) The top-view and (**E**) cross-section SEM and (F) AFM images of a NiHCF thin film show a homogenous coating of the active material. (**G**) Thickness and surface roughness of the deposited electrodes as a function of the areal capacity and mass loading. (**H**) The SEM image of NiHCF powder obtained via coprecipitation shows large secondary particles. (**I**) The XRD patterns of NiHCF thin-film and powder confirm their crystallographic similarity. The dashed lines in (**C**,**G**) serve as a guide to the eye.*

as well as *via* an electrochemical process involving the preceding reduction of $Fe(CN)_6^{3-}$

$$Fe(CN)_6^{3-} + e^- \rightarrow Fe(CN)_6^{4-} \quad \text{(eq. 2)}$$

$$Fe(CN)_6^{4-} + Ni^{2+} + 2Na^+ \rightarrow Na_2NiFe(CN)_6 \quad \text{(eq. 3)}$$

and

$$2Fe(CN)_6^{4-} + 3Ni^{2+} + 2Na^+ \rightarrow 2NaNi_{1.5}Fe(CN)_6 \quad \text{(eq. 4).}$$

According to Bácskai, the chemical step (eq. 1) can be neglected due to its slow rate compared to the electrodeposition process (eq. 3 and 4).[37] Concludingly, the film growth happens mainly during the cathodic scan of the CV, yielding a compound with mixed stoichiometry explaining the usually observed double- or shouldered-peak structure of NiHCF.[36,37,38] The growth of NiHCF thin films on the Au-QCM substrate can be directly observed by its increasing redox current response in the CV (see **Figure 2A**). The respective Na^+ (de)intercalation redox reactions can be written as follows:

$$Na_2NiFe^{II}(CN)_6 \rightleftarrows Na^+ + e^- + NaNiFe^{III}(CN)_6 \quad \text{(eq. 5)}$$

$$NaNi_{1.5}Fe^{II}(CN)_6 \rightleftarrows Na^+ + e^- + Ni_{1.5}Fe^{III}(CN)_6 \quad \text{(eq. 6)}$$

Without the restriction of generality, this manuscript will consider NiHCF as the stoichiometry described in eqs. 3 and 5.

The simultaneous EQCM measurement allows monitoring of the deposited electrode mass loading, which can be directly controlled by the number of CV cycles. **Figure 2B** shows the continuous plating of NiHCF besides a repetitive and increasing mass variation of the electrode stemming from (de)intercalating Na^+ ions. **Figure 2C** displays the obtained areal capacity over the respective mass loading for a series of NiHCF depositions up to 20 µg/cm^2. The specific capacity of the electrode material was determined to be ≈ 68 mAh/g (based on sodiated material), which matches with usually reported values.[20] The deviation from the theoretically available 85 mAh/g can be explained by defects and the non-stoichiometry of the compound due to $Fe(CN)_6^{3/4-}$ vacancies, as well as the incorporation of zeolitic and coordination water in the crystal structure.[8] The determined specific capacity was extrapolated to calculate the mass

loading for thicker films (> 20 µg/cm^2), as the QCM signal showed an increasing impact from viscous coupling for higher loadings. This can possibly damp the quartz oscillation and thereby lead to an overestimation of the deposited mass by the Sauerbrey equation. Nevertheless, there is no apparent physical or chemical reason why thicker films should have a different stoichiometry and correspondingly altered specific capacity.

The SEM images shown in **Figures 2D** and **2E** reveal a uniform and rigid deposition of the battery film on the substrate surface. A repetitive crack pattern separates the film into ≈ 1 µm sized segments, which might result from drying the film after deposition.[36] Sub-micron-sized particles on top of the film surface probably constitute precipitated NiHCF or other remains from the deposition solution precursors which formed during drying. The film surface is very homogenous and comparably smooth with a roughness in the range of 5 – 10 nm and a horizontal structure size of around 100 nm, as shown by AFM measurements (**Figure 2F and 2G**). Therefore, it can be assumed that the film consists of continuous vertical grains with an approximate diameter of ≈ 100 nm, which might be inherited from the gold substrate. As expected, **Figure 2G** confirms a linear relationship between the film-thickness and the mass loading with a 6.6 nm/(µg/cm^2) slope. Our experiments yielded the maximum possible mass loadings on plain gold substrates of approximately 100 µg/cm^2, which corresponds to ≈ 660 nm thick films. Thicker films showed low mechanical stability and even detached from the substrate in some cases.

As usually reported for the chemical synthesis routine, NiHCF precipitates as irregular nanoparticles with a size in the order of 50 nm (see **Figure 2H**).[33,39] However, these particles agglomerated to form bulky chunks extending several micrometers. This structure was maintained after the fabrication of the composite electrodes *via* slurry casting (see **Figure S2**). NiHCF powder and thin-film material yield a similar X-ray diffraction pattern matching very well with that of simulated $Na_2NiFe(CN)_6$ with a face-centered cubic $Fm\bar{3}m$ structure. Lattice constants of 10.27 Å and 10.21 Å were obtained from the (200) reflections from the thin film

and powder, respectively, which agrees with previously reported values.[20,33] Concludingly, the electrodeposition and coprecipitation routine result in a similar material without any undesired deviating side products. The higher intensity of the (111) peak obtained for the thin film might come from a preferential growth direction of the polycrystalline grains on the substrate.

Figure 3 shows the different charge and mass transport processes involved in the intercalation of sodium into NiHCF thin-film electrodes. We have shown in previous works that a simple single-step reaction cannot describe these but rather follow a complex multistep reaction with different time constants. These involve the reduction of $Fe^{III/II}$, the intermediate ad/desorption of electrolyte anions, and the insertion of Na^+ across the electrode-electrolyte interface.[31,32,40,41] This so-called "three-step-mechanism" is further explained in the supporting information. The charge propagation of the intercalated Na^+ ions within the NiHCF lattice happens *via* solid-state diffusion to entirely fill up all available sites of the active material. In general, a Na^+ desolvation step precedes the intercalation of the ion into the host material. As 8 M $NaClO_4$ was used as the electrolyte in this work to allow a degradation-free cycling of the active material,[12,13] only ≈ 2 H_2O molecules exist for each Na^+ ion. This results from the fact that the volume ratio of H_2O:solution drops to ≈ 62% due to the high amount of $NaClO_4$ salt. However, it should be mentioned that the actual structure of the solvation sheath is much more complicated than in this simplified sketch, as such "water-in-salt" electrolytes somewhat resemble a liquified salt than a classical salt solution.[42,43,44] The availability of sodium ions at the electrode surface is replenished by diffusion from the bulk electrolyte. In general, the achievable (dis)charging speed of the battery material is determined by the individual rates and complex interplay of the presented processes. In this work, we performed CV scans, galvanostatic cycling at different rates, and impedance spectroscopy to investigate the kinetics of charge and mass transport during (de)intercalation and thereby identify the rate-limiting steps for battery operation of NiHCF thin-film *vs.* composite electrodes.

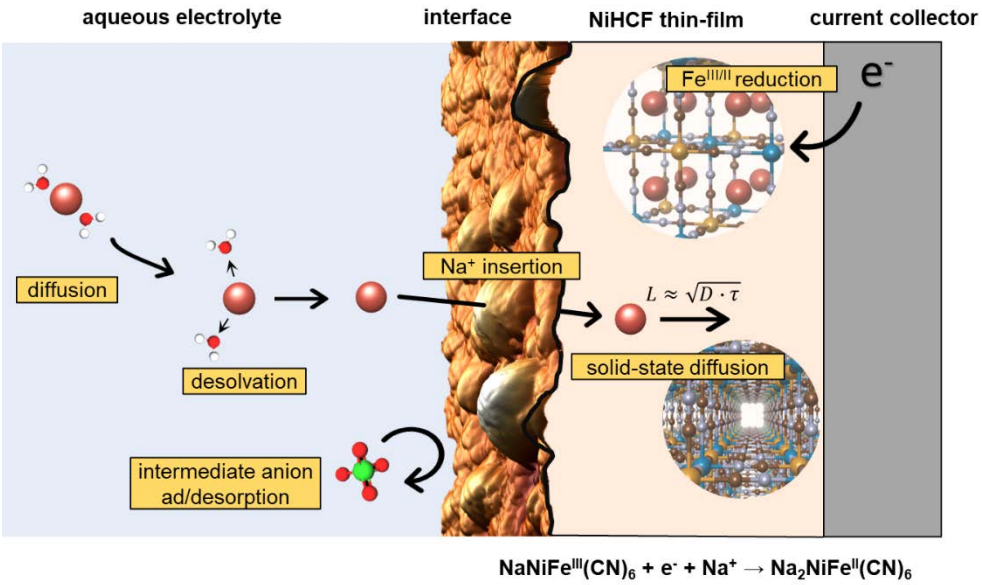

***Figure 3**. Scheme of the individual steps involved during the insertion of Na^+ ions from the electrolyte into the NiHCF electrode as a result of the $Fe^{III/II}$ reduction. It should be noted that the solvation shell only consists of a small number of H_2O molecules due to the strong hydration of the highly concentrated salt solution (8 M $NaClO_4$).*

Figure 4 shows the CVs of NiHCF thin-film electrodes with mass loadings of 10 µg/cm² (**A**), 40 µg/cm² (**B**), and 83 µg/cm² (**C**) at scan rates between 1 – 2000 mV/s. The voltammograms were corrected to compensate for the ohmic drop stemming from the uncompensated resistance, which is mostly associated with the ionic conductivity of the electrolyte. In general, the CV shape is characterized by a very reversible redox peak with $\Delta E_{peak\text{-}peak}$ in the range of a few mV for all mass loadings. From the scan-rate-normalized current curves, a linear relationship between the scan rate v and the peak current $i_{p,ox/red}$ is observed for low to medium fast cycling rates. The dependence of the peak current on the scan rate can, in general, be described by

$$i_{p,ox/red} = b \cdot v^a \rightarrow \log\left(i_{p,ox/red}\right) = a \cdot \log\left(v\right) + \log\left(b\right) \qquad \text{(eq. 7)}$$

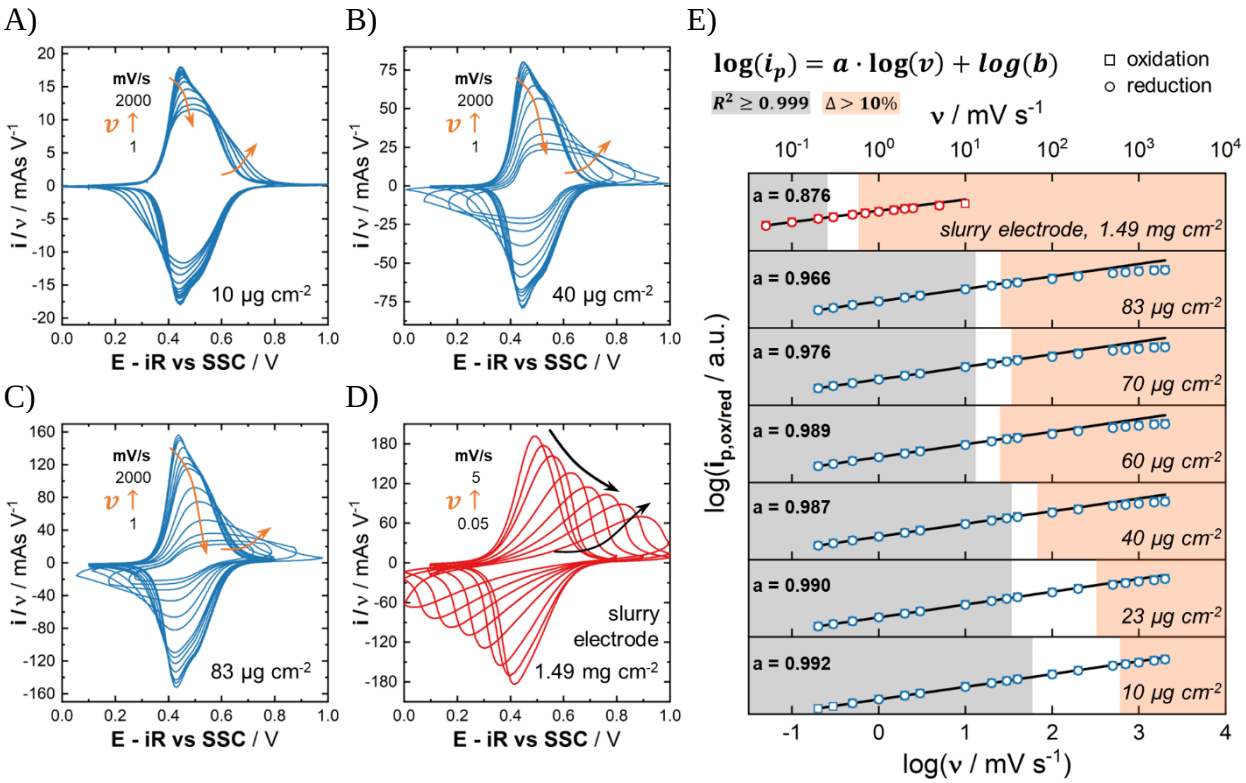

Figure 4*. Normalized CVs of (**A-C**) NiHCF thin films with varrying mass loadings and (**D**) as composite electrode at different scan rates and (**E**) the resulting dependence of the peak currents on the scan rate. For low to medium scan rates (grey-shaded area), the peak current depends linearly on the scan rate as seen from the fitting lines indicating the kinetic control of the Na^+ de/insertion.*

As shown in **Figure 4E**, a value of $a \approx 1$ is obtained over the entire range of mass loadings for the thin films up to considerably high scan rates (grey-shaded area). This linear dependency of $i(v)$ is similar to the capacitive response usually associated with the adsorption of near-surface ionic species in liquid electrolytes.[45] For the case of the herein investigated thin-film electrodes, it can be concluded that the charge transfer kinetics and the mass transport (i.e., diffusion of Na^+) are very fast and therefore do not affect the shape of CV. This implies that the coupled ion and electron transfer dynamics are governed by kinetics, i.e., the intercalation isotherm can be used to describe them.[46] The linear dependency breaks down (red-shaded area) once higher scan rates are reached. This is reflected by the contraction of the normalized CV curves and the emergence of a "tail"-like current decay after the peak potential (see arrows in **Figures 4A-C**).

The proportionality factor of **eq. 7** approaches $a \approx 0.5$, whereas $\Delta E_{peak\text{-}peak}$ increases significantly towards 50-60 mV for higher scan rates, as exemplarily shown for the 40 µg/cm² film in **Figure S3**. Such CV characteristics indicate the transition from kinetic to mass transport control for the NiHCF thin-film electrodes when increasing the scan rate.[46,47]

Remarkably, the deviation of $i \propto \nu$ is observed at lower scan rates when increasing the mass loadings of the thin-film electrodes. Considering the propagation of intercalated Na^+ ions within the host structure, it can be easily understood that solid-state diffusion constitutes the limiting process for the charging speed based on the active-material geometry and imposed rate (see **Figure 3**). Supposing that the thin-film electrode must be entirely filled up with Na^+ ions during the reduction of NiHCF, the characteristic time constant is described by

$$\tau = \frac{L^2}{D_{Na^+,NiHCF}} \qquad \text{(eq. 8)}$$

where L is the diffusion length, specified by the film thickness, and $D_{Na^+,NiHCF}$ is the diffusion coefficient of Na^+ inside NiHCF. At sufficiently high rates, the available reaction time becomes too short to maintain a uniform Na^+ concentration within the NiHCF film as the diffusion length becomes smaller than the film thickness.[36] Approximating τ by the duration of a half-cycle of the CV for the different mass loadings at the respective scan rate, where *i(ν)* shows a significant deviation from the kinetic regime (red-shaded area in **Figure 4E**), $D_{Na^+,NiHCF} \approx 10^{-11} - 10^{-10}$ cm²/s is obtained (see **Figure S4A**). Mass transport limitations stemming from the diffusion of sodium in the electrolyte can be neglected, as $D_{Na^+,solution} \approx 10^{-6} - 10^{-5}$ cm²/s in 8 M $NaClO_4$,[44] and therefore, no build-up of a Na^+ concentration gradient is expected due to its fast diffusion in the liquid phase. Furthermore, the highly concentrated solution provides an excess reservoir of Na^+ ions for intercalation in the electrode vicinity.

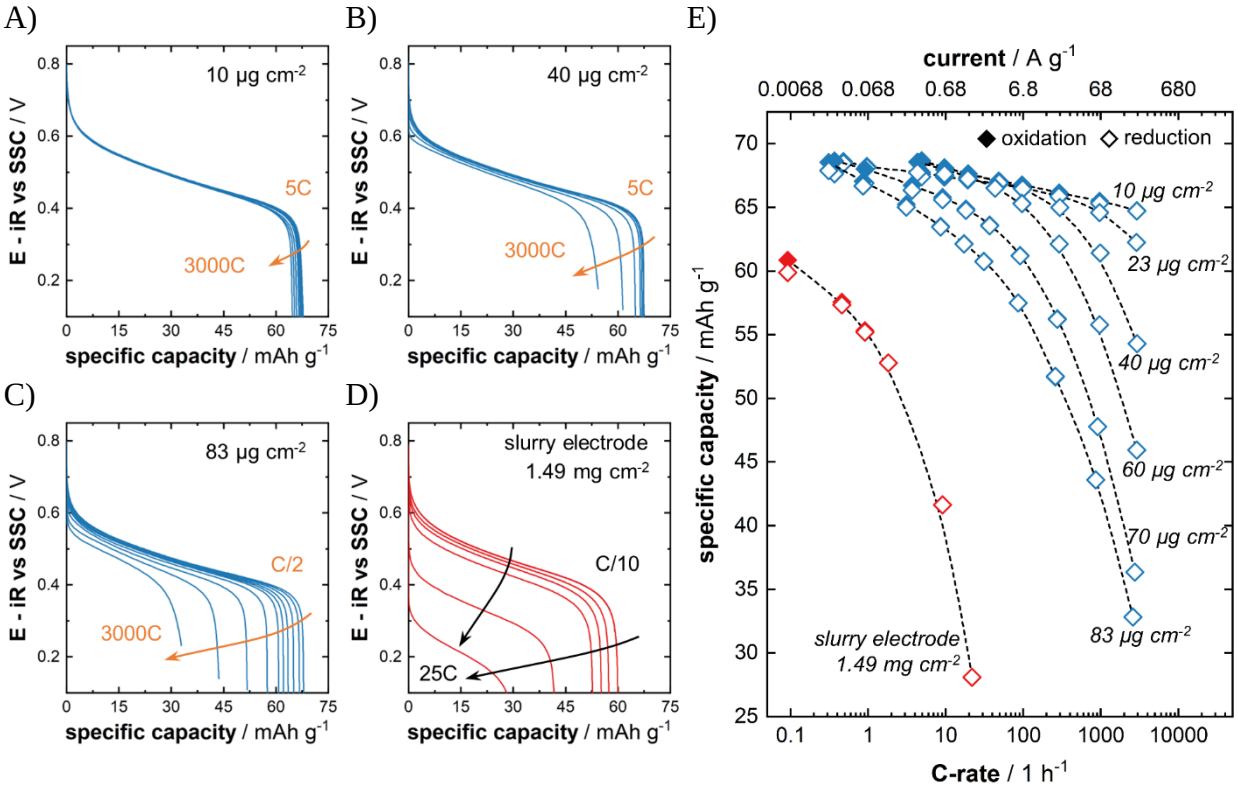

***Figure 5**. Galvanostatic discharge curves at different C-rates obtained for (**A**-**C**) NiHCF thin films with varrying mass loadings and (**D**) composite electrode. Horizontal arrows indicate the decreasing capacity, whereas the vertical arrow additionally shows the increasing hysterisis in the case of the composite electrode. (**E**) Capacity retention for a wide range of tested C-rates for the different mass loadings. The dashed lines serve as a guide to the eye.*

Analogously, we performed a set of galvanostatic cycling experiments at different rates. **Figure 5** shows the discharge curves of NiHCF thin-film electrodes with mass loadings of 10 µg/cm² (**A**), 40 µg/cm² (**B**), and 83 µg/cm² (**C**). The potentials were corrected for the uncompensated resistance. In general, all discharge curves show almost no potential hysteresis up to very high rates of 3000C. This proves that the interfacial charge transfer kinetics is fast enough not to pose a limiting factor to the system. Generally, a rate of 1C corresponds to a (dis)charging time of 1h. Sufficiently thin NiHCF film electrodes can be fully discharged within a few seconds without significant capacity losses. For higher mass loadings and, thus, thicker films, the achievable intercalation capacity drops systematically if higher C-rates are applied during discharging (**Figure 5E**). Again, this characteristic is typical for the transition to diffusional

rate control beyond "too high" (dis)charging rates. Taking a capacity threshold of $C/C_0 = 95\%$ as the transition point, where the solid-state diffusion of intercalated Na^+ ions proceeds too slowly to keep up with the imposed cycling rate, **eq. 8** yields $D_{Na^+,NiHCF} \approx 10^{-12} - 10^{-10}$ cm²/s (see **Figure S4B**), which is consistent with the values obtained from the CV data. Certainly, such treatment reflects an oversimplified model of the thin-film system. It can, therefore, only serve as an approximation, but the obtained results agree very well with diffusion coefficients reported in the literature for PBAs.[30] It should, however, be mentioned that the fast-charging capability of the thin films does not result from the high-speed diffusion properties of Na^+ within the PBA lattice but rather from the short diffusion length provided by the microstructured electrode material.[30]

In contrast to the fast cycling behavior of the NiHCF thin films, an inferior performance is found for the slurry-casted bulky electrode with probably a more commercially-relevant mass loading of 1.49 mg/cm². As shown in **Figures 4D** and **4E**, the CVs at different scan rates are characterized by a non-proportionality of $i(\nu)$ and a high $\Delta E_{peak\text{-}peak}$, which increases strongly with ν. Such behavior can be ascribed to a "mixed" rate control where both diffusion and charge transfer are slow enough to constitute limiting processes for the intercalation kinetics.[46] Similarly, the galvanostatic discharge curves at different rates exhibit severe hysteresis with increasing currents (see **Figure 5D**). The *iR*-corrected polarization curves shown in **Figure S5** represent a dependence of the overpotential as expected for a process controlled by the charge transfer kinetics (CT, η_{CT})[48]. However, since the total overpotential is $\eta - \eta_{iR} = \eta_{CT} + \eta_{diffusion}$, the individual contributions to the electrode polarization from charge transfer and mass transport cannot be differentiated without supplementary techniques.[49] Therefore, impedance spectroscopy was performed to isolate and quantify the effect of the charge transfer on the overall kinetics. **Figure S6** shows the obtained impedance spectra of a NiHCF thin-film electrode (**S6A**) and slurry electrode (**S6B**), which were fitted with a physical model describing the multistep ion de/insertion mechanism of intercalation-type battery electrodes (**S6C**, see

supporting information text for further information). The mass-normalized charge transfer resistance was found to be two orders of magnitude higher for the slurry electrode over the entire electrochemically active region of NiHCF (**Figure S6D**), consistently explaining the strong polarization of the slurry electrode by η_{CT} compared to the hysteresis-free performance of the thin-film samples.

Besides the strong hysteresis, the available capacity drops significantly for higher rates (see **Figure 5E**). A much higher rate capability would be expected, considering that the primary NiHCF particles have a size of ≈ 50 nm, which is in the order of the investigated thin-film thicknesses. Taking an approximate solid-state diffusion coefficient for intercalated sodium in the order of 10^{-11} cm²/s, the diffusion length is in the order of a few µm at a rate of 1C. Therefore Na^+ should be able to penetrate the active material entirely. However, micrometer-sized agglomerated secondary NiHCF particles were observed for both the precipitate and the composite electrodes (see **Figures 2H** and **S2**), which sufficiently explains its inferior performance as the effective diffusion pathway is extremely increased. Furthermore, these large agglomerates have a lower surface area to mass ratio compared to smaller sub-micron-sized geometries or thin films, which results in a higher mass-normalized charge transfer resistance due to the lower specific surface area available for ion de/insertion.[20,50] Therefore, the strong polarization of the slurry electrode is in accordance with its low rate capability. This effect could be further aggravated by blocking active sites for ion transfer at NiHCF particles within the composite electrode, as well as poor contact with the current collector metal foil.

Two full-cell configurations were set up and characterized to extrapolate the fast-charging properties of PBA thin-film electrodes to a battery model system. Next to NiHCF, which was used as a model system in this study, **Figure 6A** shows the CVs of sodium manganese hexacyanomanganate (MnHCM) and sodium cobalt hexacyanoferrate (CoHCF), which were obtained as thin-film electrodes *via* electrodeposition similar to NiHCF, as described in the literature.[31,51] The very low redox potential of the $Na_xMn^{II}Mn^{I/II}(CN)_6$ transition makes

MnHCM a promising anode material for ASIBs.[51,52,53,54] Similar to NiHCF. We found fast Na^+ insertion, which enables a high rate capability of MnHCM thin-film anodes (see **Figure S7**). Paired with a NiHCF cathode, a full cell discharge voltage of 1.47 V and a specific capacity of ~17.3 mAh/g is achieved based on the total active material masses of both cathode and anode, which yields an energy density of 25.5 Wh/kg (see **Figure 6B** and **6C**). The full cell reaction of the NiHCF-MnHCM battery is shown in **eq. 9**:

$$Na_2NiFe^{II}(CN)_6 + Na_2Mn^{II}Mn^{II}(CN)_6 \ (\textit{discharged})$$

$$\rightleftarrows \ NaNiFe^{III}(CN)_6 + Na_3Mn^{II}Mn^{I}(CN)_6 \ (\textit{charged}) \quad \text{(eq. 9)}$$

As shown in **Figure 6D**, the specific capacity remains constant even up to very fast rates of 360C, which corresponds to only 10 seconds for a full (dis)charge. Whereas the coulombic efficiency is ≈ 98% for the higher rates, it significantly drops when reducing the charging speed, which is reflected by a drop in the discharging capacity. We assign this detrimental behavior to parasitic HER and self-discharge reactions of the MnHCM thin-film electrode in the presence of trace amounts of oxygen in the electrolyte (see **Figures S8A-E**). Since the available surface area strictly controls the rate of both of these processes, its relative impact was observed to decrease with higher film thicknesses as the specific surface area decreases (see **Figure S8F**). Furthermore, faster (dis)charging rates leave less time for such parasitic processes, which explains why they are only observed towards lower C-rates. It should be mentioned that the employed "water-in-salt" electrolyte enables this aqueous system's extraordinarily high voltage.[43] Parasitic reactions at the low-potential anode could be even more suppressed by further electrolyte modifications to enhance its stable operation window.[55] However, further research will be necessary to optimize the reversibility of the MnHCM electrode. Nevertheless, the beneficial fast-charging behavior of the individual electrodes is maintained in the full-cell configuration. The energy density remains unaffected even at high rates, with the energy efficiency approaching 98% due to the almost negligible (dis)charge curves' hysteresis.

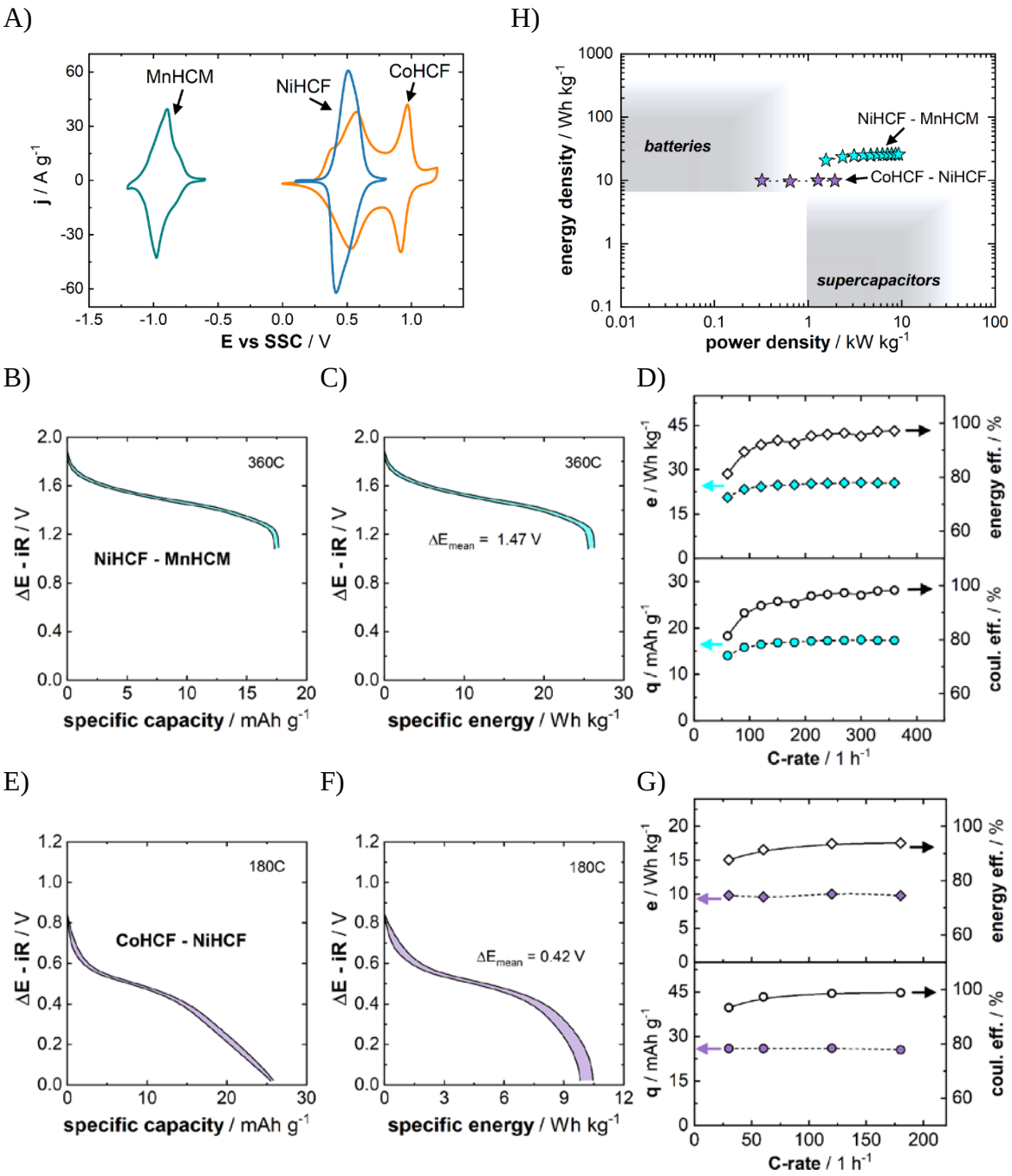

***Figure 6**. (**A**) Individual CVs of the PBA thin-film electrodes employed for assembling the two entirely PBA-based model ASIBs presented in this work. iR-corrected full cell voltage versus the specific capacity and specific energy for the NiHCF – MnHCM (**B**,**C**) and CoHCF – NiHCF (**E**,**F**) batteries at a selected high (dis)charging rate in galvanostatic mode. (**D**) and (**G**) show the respective rate capabilities of the specific discharge capacity with the corresponding coulombic efficiencies (**lower figures**) and specific energy with the corresponding energy efficiencies (**upper figures**) of the model batteries up to very high C-rates. The dashed and solid lines serve as a guide to the eye. The resulting power and energy density qualifies the presented full cells as hybrid battery-supercapacitor systems as visible from the schematic Ragone plot (**H**).*

As another example for an ASIB based on thin-film PBAs, a CoHCF cathode was paired with NiHCF, which served as the anode in this case. In general, the CV of CoHCF features a set of two redox peaks, which are associated to the activity of both $Co^{II/III}$ and $Fe^{II/III}$ in the lattice.[19] In order to maintain the full cell driving force, only the $Na_xCo^{III}Fe^{II/III}(CN)_6$ transition was allowed by restricting the individual electrode potential ranges of CoHCF and NiHCF. The mean discharge voltage of this system is 0.42 V, and a specific capacity of 26 mAh/g is obtained based on the active materials (see **Figure 6E**). As shown in **Figure 6F**, the resulting energy density is 10 Wh/kg at 180C, which results from the lower working voltage compared to the NiHCF-MnHCM cell. Nevertheless, the discharge capacity, as well as the energy density remain stable at high rates (see **Figure 6G**). Whereas a high coulombic efficiency of 98.8% is achieved at high rates, the energy efficiency is below 94%, which can be explained by irreversible processes towards the higher potential limit of the CoHCF cathode. Similar to the MnHCM anode, this effect is stronger at lower C-rates. The cell reaction is given in **eq. 10**:

$$NaCo^{III}Fe^{II}(CN)_6 + NaNiFe^{III}(CN)_6 \ (\textit{discharged})$$
$$\rightleftarrows \ Co^{III}Fe^{III}(CN)_6 + Na_2NiFe^{II}(CN)_6 \ (\textit{charged}) \quad \text{(eq. 10)}$$

Since the presented model cells can be operated at very high C-rates, the resulting power density reaches 1 – 10 kW/kg without any drop of the energy density. As visible from **Figure 6H**, this behavior qualifies such thin-film PBA materials as a hybrid battery-supercapacitor system.[24,56] Remarkably, they combine the beneficial properties of batteries, which are the provision of a stable operating voltage next to a decent energy density for an aqueous system, with the extremely high rate capability of supercapacitors. We are aware of the fact that the achieved mass loadings of the thin-film electrodes presented in this work (< 100 µg/cm²) are too low for commercially competitive batteries (several mg/cm²).[57,58] However, it should be kept in mind that the employed gold substrates for the electrodeposition had a planar geometry to allow an unambiguous characterization of the model system. By using a lightweight, conductive and microporous material as the substrate for the electrodeposition technique, the achievable total

mass loading might be increased significantly by offering a real surface largely exceeding its geometric dimensions.[16,17,59] First studies identified carbon cloth as a suitable template for the preparation of binder-free PBA electrodes.[18,60,61,62,63,64] Dedicated studies will be needed in the future to scale-up the mass loading while preserving the fast-charging capability of PBA based thin-film electrodes.

SUMMARY & CONCLUSIONS

This work aimed at elaborating the high-power properties of thin-film Prussian Blue Analogue electrodes prepared *via* a facile, single-step electrodeposition method in comparison to "traditional" composite electrodes. Their fast-charging capability was investigated by systematically varying the mass loading and, therefore, the thickness of the active material. It was found that their superior cycling performance originates from very fast charge and mass transfer kinetics. This allows a loss-free increase of the charging speed up to extremely high rates until the diffusional ion transport in the PBA lattice is no longer fast enough to fill up the entire active material. The respective rate where the electrode behavior transits to mass transport limited mode can be approximated from the diffusion coefficient and the film thickness. It was found that NiHCF electrodes with a thickness below ≈ 500 nm can be fully charged within 1 min (60C) with capacity retention above 90%. Entirely thin-film PBA-based ASIBs were assembled as model systems, showing a hysteresis- and loss-free performance even when (dis)charging the cells in less than a minute. The full cells delivered energy densities in the range of 10 – 25 Wh/kg at extremely high power densities of up to 10 kW/kg, which motivates their design as a hybrid battery-supercapacitor system.

However, further research will be necessary to increase the overall mass loading of such electrodes towards a commercially relevant scale while maintaining their beneficial fast-charging properties. Such endeavors should also improve cycling reversibility towards lower

imposed rates by suppressing parasitic reactions, a common challenge in high-voltage aqueous batteries. Microstructured, conductive templates with a high intrinsic surface area could be a promising research direction for increasing the mass loading obtained from the electrodeposition technique.

Nevertheless, the presented model systems serve as proof that thin-film PBA-based ASIBs might have great potential for high-power applications that only require a decent energy density, such as power grid stabilization or short-distance electric mobility.

Notes

The authors confirm they do not have any conflicts of interest regarding this manuscript.

Acknowledgments

Financial support from German Research Foundation (DFG) under Germany's Excellence Strategy–EXC 2089/1–390776260, cluster of excellence "e-conversion" is gratefully acknowledged. SEM and XRD analyses were carried out with the support of CEMNAT open-access Infrastructure (the Ministry of Education, Youth and Sports of the Czech Republic, LM2018103, 2020-2022).

REFERENCES

1. M. Li, J. Lu, Z. Chen, K. Amine. 30 years of lithium-ion batteries. *Advanced Materials* **2018**, *30*(33), 1800561.

2. C. Zu, Y. Ren, F. Guo, H. Yu, H. Li. A Reflection on lithium-ion batteries from a lithium-resource perspective. *Advanced Energy and Sustainability Research* **2021**, *2*(10), 2100062.

3. I. M. Peters, C. Breyer, S. A. Jaffer, S. Kurtz, T. Reindl, R. Sinton, M. Vetter. The role of batteries in meeting the PV terawatt challenge. *Joule* **2021**, *5*(6), 1353-1370.

4. B. Dunn, H. Kamath, J. M. Tarascon, Electrical energy storage for the grid: a battery of choices. *Science* **2011**, *334*(6058), 928-935.

5. M. Sawicki, L. L. Shaw. Advances and challenges of sodium ion batteries as post lithium-ion batteries. *RSC Advances* **2015**, *5*(65), 53129-53154.

6. D. Bin, F. Wang, A. G. Tamirat, L. Suo, Y. Wang, C. Wang, Y. Xia. Progress in aqueous rechargeable sodium-ion batteries. *Advanced Energy Materials* **2018**, *8*(17), 1703008.

7. J. Peng, W. Zhang, Q. Liu, J. Wang, S. Chou, H. Liu, S. Dou. Prussian blue analogues for sodium-ion batteries: past, present, and future. *Advanced Materials* **2022**, *34*(15), 2108384.

8. B. Wang, Y. Han, X. Wang, N. Bahlawane, H. Pan, M. Yan, Y. Jiang. Prussian blue analogs for rechargeable batteries. *iScience* **2018**, *3*, 110-133.

9. Q. Liu, Z. Hu, M. Chen, C. Zou, H. Jin, S. Wang, S. L. Chou, Y. Liu, S. X. Dou. The cathode choice for commercialization of sodium-ion batteries: layered transition metal oxides versus Prussian blue analogs. *Advanced Functional Materials* **2020**, *30*(14), 1909530.

10. S. Qiu, Y. Xu, X. Wu, X. Ji. Prussian blue analogues as electrodes for aqueous monovalent ion batteries. *Electrochemical Energy Reviews* **2021**, *5*(2), 242-262.

11. H. Yi, R. Qin, S. Ding, Y. Wang, S. Li, Q. Zhao, F. Pan. Structure and properties of Prussian blue analogues in energy storage and conversion applications. *Advanced Functional Materials* **2021**, *31*(6), 2006970.

12. M. Pasta, C. D. Wessells, N. Liu, J. Nelson, M. T. McDowell, R. A. Huggins, M. F. Toney, Y. Cui. Full open-framework batteries for stationary energy storage. *Nature Communications* **2014**, *5*(1), 1-9.

13. X. Lamprecht, F. Speck, P. Marzak, S. Cherevko, A.S. Bandarenka. Electrolyte effects on the stabilization of Prussian blue analog electrodes in aqueous sodium-ion batteries. *ACS Applied Materials and Interfaces* **2022**, *14*, 3515-3525.

14. B. Wang, X. Wang, C. Liang, M. Yan, Y. Jiang. An all-Prussian-blue-based aqueous sodium-ion battery. *ChemElectroChem* **2019**, *6*(18), 4848-4853.

15. P. Marzak, P. Moser, S. Schreier, D. Scieszka, J. Yun, O. Schneider, A. S. Bandarenka. A cell for controllable formation and in operando electrochemical characterization of intercalation materials for aqueous metal-ion batteries. *Small Methods* **2019**, *3*(12), 1900445.

16. G. Zhou, F. Li, H. M. Cheng. Progress in flexible lithium batteries and future prospects. *Energy & Environmental Science* **2014**, *7*(4), 1307-1338.

17. T. Jin, Q. Han, L. Jiao. Binder-free electrodes for advanced sodium-ion batteries. *Advanced Materials* **2020**, *32*(3), 1806304.

18. L. Zhang, X. Qin, S. Zhao, A. Wang, J. Luo, Z. L. Wang, F. Kang, Z. Lin, B. Li. Advanced matrixes for binder-free nanostructured electrodes in lithium-ion batteries. *Advanced Materials* **2020**, *32*(24), 1908445.

19. X. Wu, C. Wu, C. Wei, L. Hu, J. Qian, Y. Cao, X. Ai, J. Wang, H. Yang. Highly crystallized $Na_2CoFe(CN)_6$ with suppressed lattice defects as superior cathode material for sodium-ion batteries. *ACS Applied Materials & Interfaces* **2016**, *8*(8), 5393-5399.

20. S. Park, J. Kim, S. H. Yi, S. E. Chun. Coprecipitation temperature effects of morphology-controlled nickel hexacyanoferrate on the electrochemical performance in aqueous sodium-ion batteries. *ChemSusChem* **2021**, *14*(4), 1082-1093.

21. B. He, Q. Zhang, Z. Pan, L. Li, C. Li, Y. Ling, Z. Wang, M. Chen, Z. Wang, Y. Yao, Q. Ling, L. Sun, J. Wang, L. Wei. Freestanding metal–organic frameworks and their derivatives: an emerging platform for electrochemical energy storage and conversion. *Chemical reviews* **2022**, *122*, 11, 10087–10125.

22. Y. Lin, L. Zhang, Y. Xiong, T. Wei, Z. Fan, Z. Toward the design of high-performance supercapacitors by Prussian blue, its analogues and their derivatives. *Energy & Environmental Materials* **2020**, *3*(3), 323-345.

23. F. Zhang, L. Qi. Recent progress in self-supported metal oxide nanoarray electrodes for advanced lithium-ion batteries. *Advanced Science* **2016**, *3*(9), 1600049.

24. W. Zuo, R. Li, C. Zhou, Y. Li, J. Xia, J. Liu. Battery-supercapacitor hybrid devices: recent progress and future prospects. *Advanced science* **2017**, *4*(7), 1600539.

25. M. E. Şahin, F. Blaabjerg, A. Sangwongwanich. A comprehensive review on supercapacitor applications and developments. *Energies* **2022**, *15*(3), 674.

26. J. Shin, J. W. Choi. Opportunities and reality of aqueous rechargeable batteries. *Advanced Energy Materials* **2020**, *10*(28), 2001386.

27. V. D. Neff. Electrochemical oxidation and reduction of thin films of Prussian blue. *Journal of the Electrochemical Society* **1978**, *125*(6), 886.

28. K. Itaya, I. Uchida, V. D. Neff. Electrochemistry of polynuclear transition metal cyanides: Prussian blue and its analogues. *Accounts of Chemical Research* **1986**, *19*(6), 162-168.

29. A. A. Karyakin. Prussian blue and its analogues: electrochemistry and analytical applications. *Electroanalysis: An International Journal Devoted to Fundamental and Practical Aspects of Electroanalysis* **2001**, *13*(10), 813-819.

30. A. I. Komayko, N. A. Arkharova, D. E. Presnov, E. E. Levin, V. A. Nikitina. Resolving the seeming contradiction between the superior rate capability of Prussian blue analogues and the extremely slow ionic diffusion. *The Journal of Physical Chemistry Letters* **2022**, *13*(14), 3165-3172.

31. E. Ventosa, B. Paulitsch, P. Marzak, J. Yun, F. Schiegg, T. Quast, A. S. Bandarenka. The mechanism of the interfacial charge and mass transfer during intercalation of alkali metal cations. *Advanced Science* **2016**, *3*(12), 1600211.

32. J. Yun, J. Pfisterer, A. S. Bandarenka. How simple are the models of Na intercalation in aqueous media?. *Energy & Environmental Science* **2016**, *9*(3), 955-961.

33. C. D. Wessells, S. V. Peddada, R. A. Huggins, Y. Cui. Nickel hexacyanoferrate nanoparticle electrodes for aqueous sodium and potassium ion batteries. *Nano Letters* **2011**, *11*(12), 5421-5425.

34. A.S. Bandarenka. Development of hybrid algorithms for EIS data fitting. *Lecture Notes on Impedance Spectroscopy* **2013**, *4*, 29.

35. I. Horcas, R. Fernández, J.M. Gomez-Rodriguez, J. W. S. X. Colchero, J. W. S. X. M. Gómez-Herrero, A.M. Baro. WSXM: a software for scanning probe microscopy and a tool for nanotechnology. *Review of Scientific Instruments* **2007**, *78*(1), 013705.

36. X. Hao, T. Yan, Z. Wang, S. Liu, Z. Liang, Y. Shen, M. Pritzker. Unipolar pulse electrodeposition of nickel hexacyanoferrate thin films with controllable structure on platinum substrates. *Thin Solid Films* **2012**, *520*(7), 2438-2448.

37. J. Bacskai, K. Martinusz, E. Czirok, G. Inzelt, P. J. Kulesza, M. A. Malik. Polynuclear nickel hexacyanoferrates: monitoring of film growth and hydrated counter-cation flux/storage during redox reactions. *Journal of Electroanalytical Chemistry* **1995**, *385*(2), 241-248.

38. W. Chen, J. Tang, X. H. Xia. Composition and shape control in the construction of functional nickel hexacyanoferrate nanointerfaces. *The Journal of Physical Chemistry C* **2009**, *113*(52), 21577-21581.

39. H. W. Lee, M. Pasta, R. Y. Wang, R. Ruffo, Y. Cui. Effect of the alkali insertion ion on the electrochemical properties of nickel hexacyanoferrate electrodes. *Faraday Discussions* **2014**, *176*, 69-81.

40. D. Scieszka, J. Yun, A. S. Bandarenka. What do laser-induced transient techniques reveal for batteries? Na-and K-intercalation from aqueous electrolytes as an example. *ACS Applied Materials & Interfaces* **2017**, *9*(23), 20213-20222.

41. R. R. Gaddam, L. Katzenmeier, X. Lamprecht, A. S. Bandarenka. Review on physical impedance models in modern battery research. *Physical Chemistry Chemical Physics* **2021**, *23*(23), 12926-12944.

42. L. Suo, O. Borodin, Y. Wang, X. Rong, W. Sun, X. Fan, S. Xu, M. A. Schroeder, A. V. Cresce, F. Wang, C. Yang, Y. S. Hu, K. Xu, C. Wang. "Water-in-salt" electrolyte makes aqueous sodium-ion battery safe, green, and long-lasting. *Advanced Energy Materials* **2017**, *7*(21), 1701189.

43. H. Tomiyasu, H. Shikata, K. Takao, N. Asanuma, S. Taruta, Y. Y. Park. An aqueous electrolyte of the widest potential window and its superior capability for capacitors. *Scientific Reports* **2017**, *7*(1), 1-12.

44. D. A. da Silva, A. Messias, E. E. Fileti, A. Pascon, D. V. Franco, L. M. Da Silva, H. G. Zanin. Effect of conductivity, viscosity, and density of water-in-salt electrolytes on the electrochemical behavior of supercapacitors: molecular dynamics simulations and in situ characterization studies. *Materials Advances* **2022**, *3*(1), 611-623.

45. S. Y. Vassiliev, E. E. Levin, V. A. Nikitina. Kinetic analysis of lithium intercalating systems: cyclic voltammetry. *Electrochimica Acta* **2016**, *190*, 1087-1099.

46. V. A. Nikitina, S. Y. Vassiliev, K. J. Stevenson. Metal-ion coupled electron transfer kinetics in intercalation-based transition metal oxides. *Advanced Energy Materials* **2020**, *10*(22), 1903933.

47. V. V. Kondratiev, A. V. Tikhomirova, V. V. Malev. Study of charge transport processes in Prussian-blue film modified electrodes. *Electrochimica Acta* **1999**, *45*(4-5), 751-759.

48. P. L. Taberna, S. Mitra, P. Poizot, P. Simon, J. M. Tarascon. High rate capabilities Fe_3O_4-based Cu nano-architectured electrodes for lithium-ion battery applications. *Nature Materials* **2006**, *5*(7), 567-573.

49. C. Heubner, M. Schneider, A. Michaelis. Investigation of charge transfer kinetics of Li-Intercalation in $LiFePO_4$. *Journal of Power Sources* **2015**, *288*, 115-120.

50. K. Ariyoshi, M. Tanimoto, Y. Yamada. Impact of particle size of lithium manganese oxide on charge transfer resistance and contact resistance evaluated by electrochemical impedance analysis. *Electrochimica Acta* **2020**, *364*, 137292.

51. J. Yun, F. A. Schiegg, Y. Liang, D. Scieszka, B. Garlyyev, A. Kwiatkowski, T. Wagner, A. S. Bandarenka. Electrochemically formed $Na_xMn[Mn(CN)_6]$ thin film anodes demonstrate sodium intercalation and deintercalation at extremely negative electrode potentials in aqueous media. *ACS Applied Energy Materials* **2017**, *1*(1), 123-128.

52. F. Scholz, A. Dostal. The formal potentials of solid metal hexacyanometalates. *Angewandte Chemie International Edition in English* **1996**, *34*(23-24), 2685-2687.

53. A. Firouzi, R. Qiao, S. Motallebi, C. W. Valencia, H. S. Israel, M. Fujimoto, L. A. Wray, Y. D. Chuang, W. Yang, C. D. Wessells. Monovalent manganese based anodes and co-solvent electrolyte for stable low-cost high-rate sodium-ion batteries. *Nature Communications* **2018**, *9*(1), 1-10.

54. K. Hurlbutt, F. Giustino, G. Volonakis, M. Pasta. Origin of the high specific capacity in sodium manganese hexacyanomanganate. *Chemistry of Materials* **2022**, *34*(10), 4336-4343.

55. J. Xie, Z. Liang, Y. C. Lu. Molecular crowding electrolytes for high-voltage aqueous batteries. *Nature Materials* **2022**, *19*(9), 1006-1011.

56. P. Simon, Y. Gogotsi, B. Dunn. Where do batteries end and supercapacitors begin?. *Science* **2014**, *343*(6176), 1210-1211.

57. T. S. Mathis, N. Kurra, X. Wang, D. Pinto, P. Simon, Y. Gogotsi. Energy storage data reporting in perspective - guidelines for interpreting the performance of electrochemical energy storage systems. *Advanced Energy* Material **2019**s, *9*(39), 1902007.

58. Z. Lin, T. Liu, X. Ai, C. Liang. Aligning academia and industry for unified battery performance metrics. *Nature Communications* **2018**, *9*(1), 1-5.

59. B. L. Ellis, P. Knauth, T. Djenizian. Three-dimensional self-supported metal oxides for advanced energy storage. *Advanced Materials* **2014**, *26*(21), 3368-3397.

60. G. Zhang, H. Yao, F. Zhang, Z. Gao, Q. Li, Y. Yang, X. Lu. A high over-potential binder-free electrode constructed of Prussian blue and MnO_2 for high performance aqueous supercapacitors. *Nano Research* **2019**, *12*(5), 1061-1069.

61. B. He, P. Man, Q. Zhang, C. Wang, Z. Zhou, C. Li, L. Wei, Y. Yao. Conversion synthesis of self-standing potassium zinc hexacyanoferrate arrays as cathodes for high-voltage flexible aqueous rechargeable sodium-ion batteries. *Small* **2019**, *15*(52), 1905115.

62. Y. J. Yang, Y. Li, X. Ding, C. Zhang, H. Ren, F. Guo, J. Dong. Synthesis of nickel hexacyanoferrate nanostructure on carbon cloth with predeposited nickel nanoparticles as precursor for binder-free high-performance supercapacitor electrodes. *Journal of Alloys and Compounds* **2021**, *871*, 159510.

63. X. Zhang, J. Dutta. X-Fe (X= Mn, Co, Cu) Prussian blue analogue-modified carbon cloth electrodes for capacitive deionization. *ACS Applied Energy Materials* **2021**, *4*(8), 8275-8284.

64. K. Lu, B. Song, K. Li, J. Zhang, H. Ma. Cobalt hexacyanoferrate nanoparticles and MoO_3 thin films grown on carbon fiber cloth for efficient flexible hybrid supercapacitor. *Journal of Power Sources* **2017**, *370*, 98-105.